Collision-geometry-based 3D initial condition for relativistic heavy-ion collisions

Chun Shen [1,2,*] and Sahr Alzhrani [1,3,†]

[1]*Department of Physics and Astronomy, Wayne State University, Detroit, Michigan 48201, USA*
[2]*RIKEN BNL Research Center, Brookhaven National Laboratory, Upton, New York 11973, USA*
[3]*Department of Physics, Jazan University, Jazan, Kingdom of Saudi Arabia*

(Received 20 March 2020; accepted 30 June 2020; published 15 July 2020)

We present a simple way to construct three-dimensional initial conditions for relativistic heavy-ion collisions based on the Glauber collision geometry. Local energy and momentum conservation conditions are imposed to set non-trivial constraints on our parametrizations of longitudinal profiles for the system's initial energy density and flow velocity. After calibrating parameters with charged hadron rapidity distributions in central Au + Au collisions, we test model predictions for particle rapidity distributions in d + Au and peripheral Au + Au collisions in the Beam Energy Scan program at the Relativistic Heavy-Ion Collider. Simulations and comparisons with measurements are also made for Pb + Pb collisions at Super Proton Synchrotron energies. We demonstrate that elliptic flow measurements in heavy-ion collisions at $\sqrt{s} \sim 10$ GeV can set strong constraints on the dependence of quark-gluon plasma shear viscosity on temperature and net baryon chemical potential.

DOI: 10.1103/PhysRevC.102.014909

I. INTRODUCTION

Understanding the phase structure of QCD matter is one of the critical questions in relativistic heavy-ion physics. First-principles lattice QCD calculations have established that the transition from hadron resonance gas to the quark-gluon plasma (QGP) phase at vanishing net baryon density is a smooth crossover [1]. The presence of a first-order transition accompanied by a critical point at some finite net baryon density has been conjectured based on many model calculations (see, e.g., Refs. [2,3] for a review). Current heavy-ion experiments in the Relativistic Heavy-Ion Collider (RHIC) Beam Energy Scan (BES) program, the NA61/SHINE experiment at the Super Proton Synchrotron (SPS), as well as future experiments at the Facility for Antiproton and Ion Research (FAIR) and Nuclotron-based Ion Collider Facility (NICA), produce hot and dense nuclear matter to probe an extensive temperature and baryon chemical potential region in the QCD phase diagram. Measurements from these collisions study the nature of the QCD phase transition from hadron gas to the QGP at different net baryon densities. Furthermore, the STAR Collaboration at the RHIC discovered non-zero global polarization of Λ hyperons, which could indicate local fluid vorticity of $\omega \approx (9 \pm 1) \times 10^{21}\ \mathrm{s}^{-1}$ [4]. This result far surpasses the vorticity of all other known fluids in nature. Hence, it is of great interest to understand the origin of the RHIC Λ polarization measurements. Because the tiny fireballs created in heavy-ion collisions undergo ultra-fast yoctosecond dynamics, theoretical modeling of the system's multi-stage evolution is essential to elucidate physics from experimental measurements. In particular, phenomenological studies of precise flow measurements of the hadronic final states allow for the extraction of transport properties of the QGP in a baryon-rich environment [5].

Heavy-ion collisions at $\sqrt{s} \sim \mathcal{O}(10)$ GeV strongly violate longitudinal boost invariance and require full three-dimensional (3D) modeling of their dynamics [6]. The geometry of incoming nuclei and the impact parameter between them determines the transverse shape of the produced fireball at a length scale of system size. Event-by-event fluctuations raise at multiple smaller length scales, such as nucleon-size fluctuations from random positions of nucleons inside the colliding nucleus [7] and sub-nucleon fluctuations from valence quarks and gluon fields [8–10]. Recently, there is a collective interest in understanding the longitudinal dynamics of heavy-ion collisions. The longitudinal profile of initial energy density is usually parametrized by a plateaulike function in symmetric collision systems [11]. Variations of parametrizations were proposed to study the rapidity-dependent directed flow as well as longitudinal flow fluctuations [12–16]. Models that include 3D dynamical evolution at the pre-hydrodynamic phase were recently developed based on classical strings deceleration [6,17] and transport approaches [18–21]. These models can provide a non-trivial correlation between the rapidity and space-time rapidity of energy-momentum and net baryon density currents [22]. These models have predictive power for particle rapidity distributions at different collision energies. In addition, there are new theoretical developments in exploring longitudinal flow observables with the (3 + 1)D IP-Glasma model [23,24], understanding early-stage baryon stopping from color glass condensate (CGC) effective-theory-based approaches in the fragmentation region [25,26], and from a holographic approach at intermediate couplings [27].

In this work, we assume that all the energy and momentum from the two colliding nuclei are deposited into fluid dynamic

*chunshen@wayne.edu
†sahr.alzhrani@wayne.edu

fields in 3D hydrodynamic simulations. Rare processes, such as QCD jets and heavy-quark productions, carry negligible energy and momentum compared to those of the entire collision system. Using these constraints from total energy and net longitudinal momentum, we can reduce the number of model parameters in longitudinal profiles for the initial energy density. Specifically, we do not require an overall normalization factor for the system's initial energy density profile anymore. By adjusting the width of the energy density plateau to match the measured charged hadron multiplicity at midrapidity, this model can make predictions for the centrality dependence of particle production as well as particle rapidity distributions. A similar idea was proposed in Ref. [28] to study the particle production at the top SPS collision energy. In this work, we find that imposing local energy-momentum conservation in 3D initial conditions can lead to a non-trivial transverse energy density profile. Our proposed scheme can straightforwardly extend to event-by-event simulations in the future. Because this approach ignored pre-equilibrium dynamics during the two colliding nuclei passing through each other, our results serve as a baseline for future comparisons with more realistic dynamical initialization frameworks.

In the next section, we describe the procedure of imposing local energy-momentum conservation and our parametrization of longitudinal profiles. Using event-averaged density profiles for nuclear thickness functions, we analyze the longitudinal distribution and collision centrality dependence of the fireball's initial eccentricity coefficients. Section III presents our theoretical results from evolving 3D initial conditions with hydrodynamics plus a hadronic transport hybrid framework. We present a phenomenological study compared with experimental measurements at RHIC BES and SPS programs, focusing on charged hadron and identified particle rapidity distributions. The particle's directed and elliptic flow coefficients are studied as well. Section IV is devoted to some concluding remarks.

II. THE MODEL FRAMEWORK

In this section, we discuss an extension of geometry-based two-dimensional (2D) initial conditions to three dimensions with parametric longitudinal profiles for energy and net baryon densities. Conservation laws of local energy and momentum are imposed to constrain our parametrization.

A. Local energy-momentum conservation

The nucleus thickness function determines collision geometry in the transverse plane:

$$T_{A(B)}(x,y) = \sum_{i\in\text{participants}} \frac{1}{2\pi\sigma_\perp^2} \exp\left[-\frac{(x-x_i)^2}{2\sigma_\perp^2} - \frac{(y-y_i)^2}{2\sigma_\perp^2}\right]. \tag{1}$$

We denote the colliding nucleus A as the projectile, which has a positive velocity along the longitudinal direction, and the nucleus B to fly to negative a direction as the target. The impact parameter vector $\vec{b}$ is defined to start from the target to the projectile. Individual nucleons are assumed to have a Gaussian profile in the transverse plane with a parametric width of $\sigma_\perp$. Before the collision, all the nucleons fly with the beam rapidity determined by the center-of-mass collision energy $\sqrt{s_{\rm NN}}$,

$$y_{\rm beam} = \text{arccosh}\left(\frac{\sqrt{s_{\rm NN}}}{2m_N}\right). \tag{2}$$

Here the nucleon mass is m_N. With nucleus thickness functions, we can determine the local collision energy and net longitudinal momentum at any point in the transverse plane (x, y):

$$\begin{aligned} E(x,y) &= [T_A(x,y) + T_B(x,y)]m_N \cosh(y_{\rm beam}) \\ &\equiv M(x,y)\cosh(y_{\rm CM}(x,y)), \end{aligned} \tag{3}$$

$$\begin{aligned} P_z(x,y) &= [T_A(x,y) - T_B(x,y)]m_N \sinh(y_{\rm beam}) \\ &\equiv M(x,y)\sinh(y_{\rm CM}(x,y)). \end{aligned} \tag{4}$$

We can define a local invariant mass $M(x, y)$ and a center-of-mass rapidity $y_{\rm CM}(x, y)$:

$$y_{\rm CM}(x,y) = \text{arctanh}\left[\frac{T_A - T_B}{T_A + T_B}\tanh(y_{\rm beam})\right], \tag{5}$$

$$M(x,y) = m_N\sqrt{T_A^2 + T_B^2 + 2T_AT_B\cosh(2y_{\rm beam})}. \tag{6}$$

These conditions are used to constrain the longitudinal profiles at matching between initial conditions and hydrodynamic fields. It is worth noting that the factor $\cosh(2y_{\rm beam}) \gg 1$ for $\sqrt{s_{\rm NN}} > 5$ GeV. At these collision energies, the local invariant mass at a transverse point (x, y) is proportional to $\sqrt{T_A(x,y)T_B(x,y)}$.

At the beginning of hydrodynamic simulations, we consider hydrodynamic initial conditions on a constant proper time surface $\tau \equiv \sqrt{t^2 - z^2} = \tau_0$:

$$\begin{aligned} M(x,y)\cosh[y_{\rm CM}(x,y)] &= \int d^3\Sigma_\mu T^{\mu t}(x,y,\eta_s) \\ &= \int \tau_0 d\eta_s (T^{\tau\tau}(x,y,\eta_s)\cosh(\eta_s) \\ &\quad + \tau_0 T^{\tau\eta}(x,y,\eta_s)\sinh(\eta_s)), \end{aligned} \tag{7}$$

$$\begin{aligned} M(x,y)\sinh[y_{\rm CM}(x,y)] &= \int d^3\Sigma_\mu T^{\mu z}(x,y,\eta_s) \\ &= \int \tau_0 d\eta_s (T^{\tau\tau}(x,y,\eta_s)\sinh(\eta_s) \\ &\quad + \tau_0 T^{\tau\eta}(x,y,\eta_s)\cosh(\eta_s)). \end{aligned} \tag{8}$$

Here $T^{\tau\tau}(x, y, \eta_s)$ and $T^{\tau\eta}(x, y, \eta_s)$ are components of the system's energy-momentum tensor at $\tau = \tau_0$. We can rewrite Eqs. (7) and (8) as follows:

$$\begin{aligned} M(x,y) &= \int \tau_0 d\eta_s (T^{\tau\tau}\cosh(\eta_s - y_{\rm CM}) \\ &\quad + \tau_0 T^{\tau\eta}\sinh(\eta_s - y_{\rm CM})), \end{aligned} \tag{9}$$

$$\begin{aligned} 0 &= \int \tau_0 d\eta_s (T^{\tau\tau}\sinh(\eta_s - y_{\rm CM}) \\ &\quad + \tau_0 T^{\tau\eta}\cosh(\eta_s - y_{\rm CM})). \end{aligned} \tag{10}$$

These two equations suggest that $T^{\tau\tau}(\eta_s)$ should be an even function to $y_{\rm CM}$ and $\tau_0 T^{\tau\eta}(\eta_s)$ is odd with respect to $y_{\rm CM}$. In general, when we choose longitudinal profiles for local energy density and flow velocity profiles, we need to ensure conservation of energy and momentum in Eqs. (7) and (8). These two conditions can eliminate two degrees of freedom in the model parameter space.

B. A simple parametrization of longitudinal profiles for local energy density and flow velocity

To keep our model simple, we assume the Bjorken flow for the system's flow velocity profile at $\tau = \tau_0$:

$$u^\mu(x, y, \eta_s) = (\cosh(\eta_s), 0, 0, \sinh(\eta_s)). \tag{11}$$

This assumption significantly reduces the complexity of the system's initial energy-momentum tensor, making it only a function of the local energy density, $T^{\tau\tau}(x, y, \eta_s) = e(x, y, \eta_s)$ and $T^{\tau\eta} = 0$. Energy-momentum conservation leads to

$$M(x, y) = \int \tau_0 d\eta_s e(x, y, \eta_s) \cosh(\eta_s - y_{\rm CM}), \tag{12}$$

$$0 = \int \tau_0 d\eta_s e(x, y, \eta_s) \sinh(\eta_s - y_{\rm CM}). \tag{13}$$

We choose a symmetric rapidity profile parametrization with respect to $y_{\rm CM}$ for the local energy density [11],

$$e(x, y, \eta_s; y_{\rm CM}) = \mathcal{N}_e(x, y) \exp\left[-\frac{(|\eta_s - y_{\rm CM}| - \eta_0)^2}{2\sigma_\eta^2} \times \theta(|\eta_s - y_{\rm CM}| - \eta_0)\right]. \tag{14}$$

Here the parameter η_0 determines the width of the plateau and the σ_η controls how fast the energy density falls off at the edge of the plateau. In a highly asymmetric situation $T_A(x, y) \gg T_B(x, y)$, the center-of-mass rapidity $y_{\rm CM}(x, y) \to y_{\rm beam}$. To make sure there is not too much energy density deposited beyond the beam rapidity, we set $\eta_0(x, y) = \min(\eta_0, y_{\rm beam} - y_{\rm CM}(x, y))$. The normalization factor $\mathcal{N}_e(x, y)$ is not a free parameter in our model. It is determined by the local invariant mass $M(x, y)$,

$$\mathcal{N}_e(x, y) = \frac{M(x, y)}{2\sinh(\eta_0) + \sqrt{\frac{\pi}{2}}\sigma_\eta e^{\sigma_\eta^2/2} C_\eta}, \tag{15}$$

$$C_\eta = e^{\eta_0}\mathrm{erfc}\left(-\sqrt{\frac{1}{2}}\sigma_\eta\right) + e^{-\eta_0}\mathrm{erfc}\left(\sqrt{\frac{1}{2}}\sigma_\eta\right). \tag{16}$$

Here $\mathrm{erfc}(x)$ is the complementary error function. Because the local invariant mass $M(x, y) \propto \sqrt{T_A(x, y) T_B(x, y)}$, our choice of the longitudinal profile leads to local energy density $e(x, y) \propto \sqrt{T_A(x, y) T_B(x, y)}$ inside the plateau region. At the top RHIC and Large Hadron Collider (LHC) energy, the plateau width η_0 is large. Our derivation suggests that the transverse energy density in the mid-rapidity region should scale with $\sqrt{T_A(x, y) T_B(x, y)}$ instead of the participant nucleon profile or binary collision profile. The scaling with $\sqrt{T_A(x, y) T_B(x, y)}$ was preferred from the current state-of-the-art Bayesian extraction [29,30]. Our model provides a physics explanation that this scaling is rooted from conservation of energy and longitudinal momentum.

TABLE I. The model parameters for longitudinal envelope profiles for the system's local energy density and net baryon density.

$\sqrt{s_{\rm NN}}$ (GeV)	τ_0 (fm/c)	η_0	σ_η	$\eta_{B,0}$	$\sigma_{B,\rm in}$	$\sigma_{B,\rm out}$
Au+Au and d + Au at 200	1.0	2.5	0.6	3.5	2.0	0.1
Au+Au and d + Au at 62.4	1.0	2.25	0.3	2.7	1.9	0.2
Au+Au and d + Au at 39	1.3	1.9	0.3	2.2	1.6	0.2
Au+Au at 27	1.4	1.6	0.3	1.8	1.5	0.2
Au+Au and d + Au at 19.6	1.8	1.3	0.3	1.5	1.2	0.2
Au+Au at 14.5	2.2	1.15	0.3	1.4	1.15	0.2
Au+Au at 7.7	3.6	0.9	0.2	1.05	1.0	0.1
Pb+Pb at 17.3	1.8	1.25	0.3	1.6	1.2	0.2
Pb+Pb at 8.77	3.5	0.95	0.2	1.2	1.0	0.1

We prepare event-averaged nuclear thickness functions based on the Monte Carlo Glauber model using the open-source code package SUPERMC within the IEBE-VISHNU framework [31,32]. Centrality classes are determined with the number of participating nucleons in each collision. Over 10 000 fluctuating initial conditions in every centrality bin are averaged after rotating each event by its second-order participant plane angle to align the respective eccentricities [33,34].

We use the same net baryon density profile as was used in Ref. [35]:

$$f^A_{n_B}(\eta_s) = \mathcal{N}_{n_B}\left\{\theta(\eta_s - \eta_{B,0}) \exp\left[-\frac{(\eta_s - \eta_{B,0})^2}{2\sigma^2_{B,\rm out}}\right] + \theta(\eta_{B,0} - \eta_s) \exp\left[-\frac{(\eta_s - \eta_{B,0})^2}{2\sigma^2_{B,\rm in}}\right]\right\} \tag{17}$$

and

$$f^B_{n_B}(\eta_s) = \mathcal{N}_{n_B}\left\{\theta(\eta_s + \eta_{B,0}) \exp\left[-\frac{(\eta_s + \eta_{B,0})^2}{2\sigma^2_{B,\rm in}}\right] + \theta(-\eta_{B,0} - \eta_s) \exp\left[-\frac{(\eta_s + \eta_{B,0})^2}{2\sigma^2_{B,\rm out}}\right]\right\}. \tag{18}$$

Table I summarizes the values of model parameters for the longitudinal profiles in Eqs. (14), (17), and (18). They are calibrated with charged hadron and net proton rapidity distributions in central Au + Au collisions at different collision energies. With these parameters, we illustrate a 3D local energy density distribution for 20–30% Au + Au collisions at $\sqrt{s_{\rm NN}} = 19.6$ GeV in Fig. 1. Because the two colliding nuclei are offset by a finite impact parameter, their nuclear thickness functions at the edge of the overlapping region are not symmetric. This asymmetry shifts the local energy density plateau by a space-time rapidity $\Delta\eta_s = y_{\rm CM}(x, y)$ along the longitudinal direction. This effect makes a wider longitudinal distribution for energy density when collisions are asymmetric in the transverse plane. Figures 1(b)–1(d) further show that the transverse shape of the energy density becomes more eccentric at forward and backward rapidity regions.

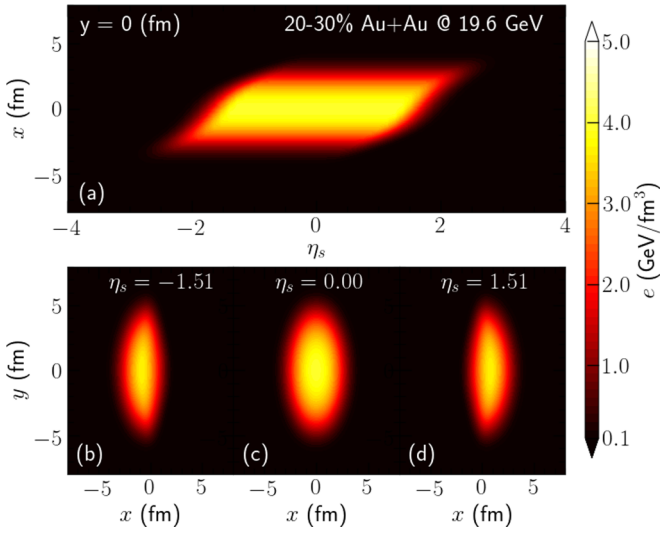

FIG. 1. Color contour plot for the local energy density distribution at $\tau = 1.8$ fm/c in 20–30% Au + Au collisions at 19.6 GeV.

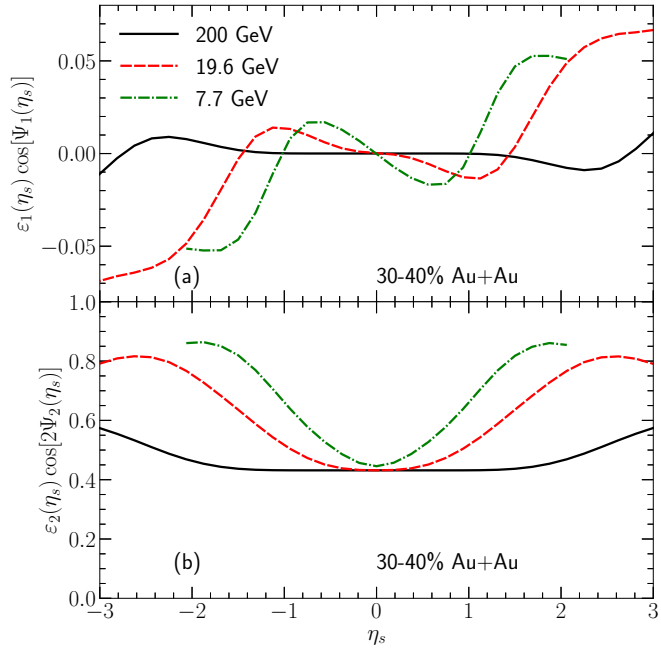

FIG. 2. The space-time rapidity distribution of initial eccentricity coefficients $\varepsilon_1(\eta_s)$ and $\varepsilon_2(\eta_s)$ for 30–40% Au + Au collisions at 200, 19.6, and 7.7 GeV.

C. Boost-invariance-breaking effects on fireballs' transverse geometry

Before we perform hydrodynamic simulations, it is instructive to study the dependence of collision systems' initial eccentricities on centrality and space-time rapidity. The initial eccentricity coefficients can be defined as

$$\vec{\mathcal{E}}_1 \equiv \varepsilon_1(\eta_s)e^{i\Psi_1(\eta_s)} = -\frac{\int d^2r\tilde{r}^3 e^{i\tilde{\phi}}e(r,\phi,\eta_s)}{\int d^2r\tilde{r}^3 e(r,\phi,\eta_s)}, \tag{19}$$

$$\vec{\mathcal{E}}_n \equiv \varepsilon_n(\eta_s)e^{in\Psi_n(\eta_s)} = -\frac{\int d^2r\tilde{r}^n e^{in\tilde{\phi}}e(r,\phi,\eta_s)}{\int d^2r\tilde{r}^n e(r,\phi,\eta_s)} \quad \text{for } (n \geqslant 2). \tag{20}$$

Here we compute those eccentricity coefficients with respect to the energy density weighted center-of-mass point $(x_0(\eta_s), y_0(\eta_s))$ in every space-time rapidity slice. The transverse radius and azimuthal angle are defined as $\tilde{r}(x,y,\eta_s) = \sqrt{(x-x_0(\eta_s))^2 + (y-y_0(\eta_s))^2}$ and $\tilde{\phi}(x,y,\eta_s) = \arctan[(y - y_0(\eta_s))/(x - x_0(\eta_s))]$. The center-of-mass point is computed using local energy density as a weight:

$$x_0(\eta_s) = \frac{\int d^2rxe(r,\phi,\eta_s)}{\int d^2re(r,\phi,\eta_s)}, \tag{21}$$

$$y_0(\eta_s) = \frac{\int d^2rye(r,\phi,\eta_s)}{\int d^2re(r,\phi,\eta_s)}. \tag{22}$$

The space-time rapidity distribution of initial eccentricity vectors is demonstrated in Fig. 2 for 30–40% Au + Au collisions at 7.7, 19.6, and 200 GeV. We set the impact parameter to point along the $+x$ direction so that the imaginary part of $\vec{\mathcal{E}}_n$ is zero. The dipole deformation vector $\vec{\mathcal{E}}_1(\eta_s)$ is an odd function in space-time rapidity, which reflects shape variations of transverse energy density profiles along the η_s direction shown in Fig. 1. Collisions at lower energy show stronger dipole deformations. At 19.6 GeV, the dipole vector $\vec{\mathcal{E}}_1(\eta_s)$ points to the direction where the colliding nucleus sits in the transverse plane in a forward region with $\eta_s > 1.4$. In this region, the shape of local energy density is dominated by the projectile nuclear thickness function. In the meantime, the direction of $\vec{\mathcal{E}}_1(\eta_s)$ is opposite near the mid-rapidity region, $|\eta_s| < 1.4$. Figure 1(d) shows that the shape of the target nuclear thickness function generates the steepest gradient in the local energy density profile at $\eta_s \sim 1.5$. It flips the dipole vector's direction.

The initial $\vec{\mathcal{E}}_2(\eta_s)$ vector is an even function in space-time rapidity. At 200 GeV, the magnitude of elliptic deformation $\varepsilon_2(\eta_s)$ remains constant for a space-time rapidity window of $\eta_s \sim [-1.5, 1.5]$, showing approximated boost invariance in this region. Such a plateau region shrinks quickly as collision energy decreases. The spatial ellipticity increases in forward and backward rapidity regions because of the shifts induced by the local net longitudinal momentum. This is consistent with those energy density profiles illustrated in Figs. 1(b)–1(d).

In Fig. 3, we further study the centrality dependence of ε_2 at mid-rapidity in Au + Au collisions at four collision energies. They are compared with those eccentricities estimated with different functions of the two nuclear thickness functions. The case $\varepsilon_2(T_A + T_B)$ corresponds to the ellipticity of the participant nucleon profile, while the results from $\varepsilon_2(T_AT_B)$ represent the quadruple deformation of the system's binary collision profile. Based on our derivation in the previous section, our eccentricity ϵ_2^{3D} at $\eta_s = 0$ should approximately scale with the $\sqrt{T_AT_B}$ profile. With the model parameters listed in Table I, we find the $\sqrt{T_AT_B}$ eccentricity scaling works well even at $\sqrt{s} = 7.7$ GeV.

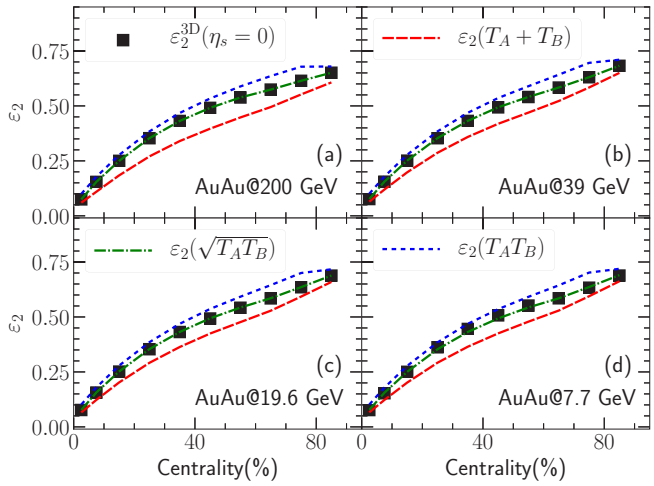

FIG. 3. Centrality dependence of the initial eccentricity ε_2 for Au + Au collisions at 200, 39, 19.6, and 7.7 GeV. The mid-rapidity eccentricities from 3D energy density profiles are compared with those assuming longitudinal boost invariance and local energy density being proportional to $T_A + T_B$, $\sqrt{T_AT_B}$, and T_AT_B. Here T_A and T_B are the nuclear thickness functions.

D. Temperature- and net-baryon-chemical-potential-dependent QGP specific shear viscosity

The 3D energy density and net baryon density profiles serve as initial conditions for hydrodynamics and hadronic transport simulations. In this work, we use the open-source 3D viscous hydrodynamic code package MUSIC [35–39] to simulate fluid dynamical evolution of the collision system's energy, momentum, and net baryon density:

$$\partial_\mu T^{\mu\nu} = 0, \tag{23}$$

$$\partial_\mu J_B^\mu = 0. \tag{24}$$

Because the overlapping time for the two colliding nuclei to pass through each other is not negligible at $\sqrt{s} \sim \mathcal{O}(10)$ GeV [6,19], we start our hydrodynamic simulations at $\tau = \tau_0 > \tau_{\rm overlap}$. The values of τ_0 used at different collision energies are listed in Table I. They are calibrated to reproduce the measured identified particle mean p_T in Au + Au collisions. Hydrodynamic equations of motion are solved with a lattice-QCD-based equation of state (EoS) at finite net baryon density, NEoS-BQS [40,41]. This EoS imposes strangeness neutrality and constrains the local net electric charge density to be 0.4 times the local net baryon density. We include shear viscous effects during hydrodynamic simulations. We explore a temperature- and net-baryon-chemical-potential-dependent specific shear viscosity $(\eta/s)(T, \mu_B)$, which is parametrized as

$$\frac{\eta}{s}(T,\mu_B) = \left(\frac{\eta}{s}\right)_0 f_T(T)\left(\frac{e+P}{Ts}\right) f_{\mu_B}(\mu_B). \tag{25}$$

Here the temperature- and net-baryon-chemical-potential-dependent $(\eta/s)(T, \mu_B)$ is defined via the following functions:

$$f_T(T) = 1 + T_{\rm slope}\frac{T - T_c}{T_c - T_{\rm low}}\theta(T_c - T) \tag{26}$$

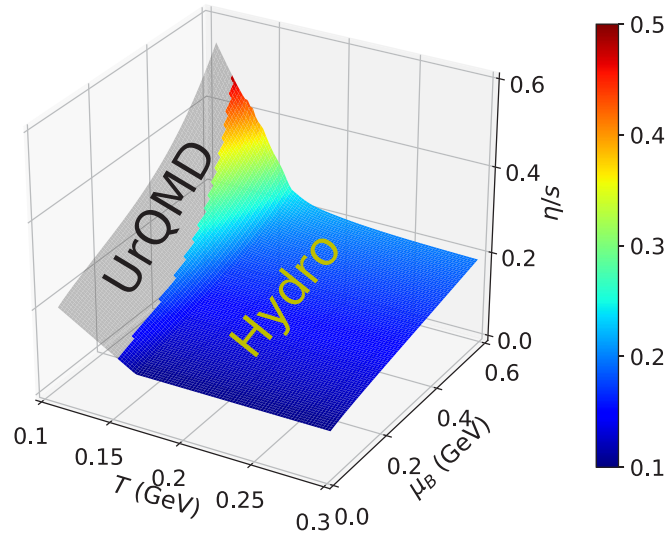

FIG. 4. The specific shear viscosity $(\eta/s)(T, \mu_B)$ used in our hydrodynamic simulations. The grey area indicates the hadronic transport region with $e_{\rm sw} < 0.26$ GeV/fm^3.

and

$$f_{\mu_B}(\mu_B) = 1 + \mu_{B,\rm slope}\left(\frac{\mu_B}{\mu_{B,\rm scale}}\right)^\alpha. \tag{27}$$

In addition, the factor $(e + P)/(Ts)$ introduces some extra T and μ dependence through the equation of state NEoS-BQS ($n_S = 0, n_Q = 0.4n_B$) at finite densities:

$$\frac{e+P}{Ts} = 1 + \sum_{i=B,Q,S}\frac{n_i}{s}\frac{\mu_i}{T} = 1 + \frac{n_B}{s}\frac{\mu_B + 0.4\mu_Q}{T}. \tag{28}$$

Calibrating our full hybrid simulations with charged hadron elliptic flow measurements at the RHIC BES program (see results in Sec. III D below), we find the following set of parameters: $(\eta/s)_0 = 0.1$, $T_c = 0.165$ GeV, $T_{\rm low} = 0.1$ GeV, $T_{\rm slope} = 1.2$, $\mu_{B,\rm slope} = 0.9$, $\mu_{B,\rm scale} = 0.6$ GeV, and $\alpha = 0.8$.

Figure 4 shows the temperature- and net-baryon-chemical-potential-dependent specific shear viscosity $(\eta/s)(T, \mu_B)$ used in our hydrodynamic simulations. It increases rapidly at low temperature and in large-μ_B regions. Our hydrodynamic simulations transition to a microscopic transport description, URQMD [42,43], on a constant energy density hyper-surface with $e_{\rm sw} = 0.26$ GeV/fm^3. The hadronic transport phase is indicated as the grey area in Fig. 4.

III. RESULTS AND DISCUSSIONS

In this section, we present our model calibrations and test its predictions with measurements in the RHIC BES and the CERN SPS programs. Our results serve as a baseline for future comparisons with more realistic event-by-event simulations with a dynamical initialization scheme [6].

A. Particle productions and their rapidity distributions

While the overall normalization of our longitudinal profile for energy density is constrained by the system's collision

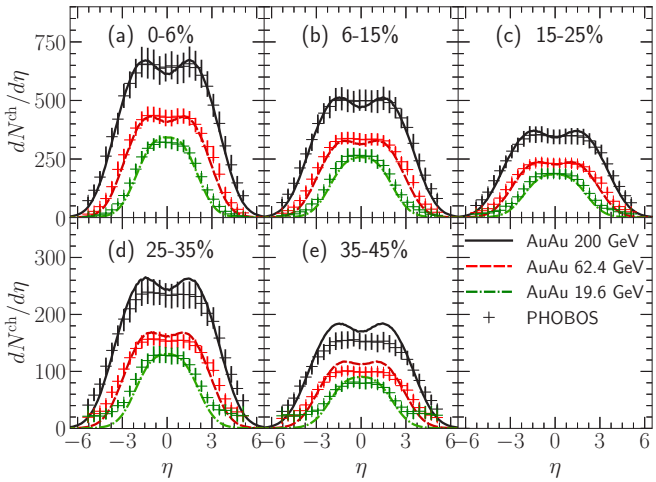

FIG. 5. Pseudorapidity distributions of charged hadron production are compared with the PHOBOS measurements in Au + Au collisions at 19.6, 62.4, and 200 GeV [44].

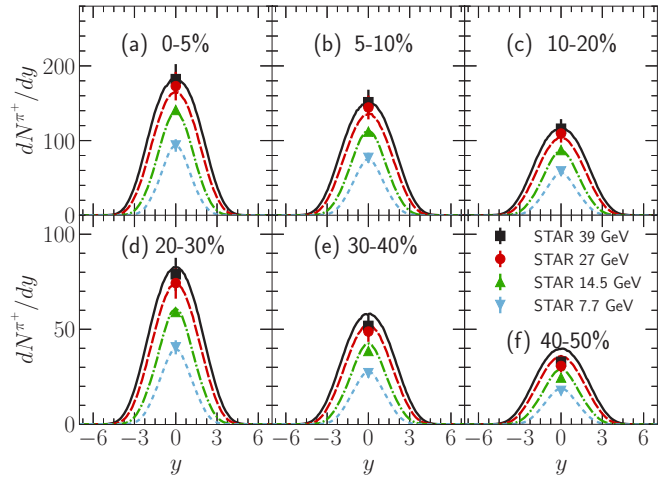

FIG. 6. Rapidity distributions of π^+ are compared with the STAR measurements in Au + Au collisions at 7.7, 14.5, 27, and 39 GeV [45].

energy in Eq. (14), the widths of energy density plateaus at different $\sqrt{s}$ need to be calibrated with measured charged hadron pseudorapidity distributions.

Figure 5 shows a comparison of charged hadron pseudorapidity distributions between our model and the PHOBOS measurements in Au + Au collisions at 19.6, 62.4, and 200 GeV [44]. We only use the most central 0–6% centrality data for model calibrations. Comparisons in the other four centrality bins test our model predictions. The dependence of particle production on centrality is well reproduced with our 3D initial conditions. We find that the rapidity boost to energy density profiles from the longitudinal momentum constraint in Eq. (5) plays a crucial role in reproducing the measured centrality dependence of particle yields. The asymmetry between the two nuclear thickness functions at a given transverse position is larger in peripheral centrality bins compared to those in central collisions. The larger asymmetry at the edge of the transverse overlapping area boosts more energy density to forward and backward rapidity regions. This effect leads to a wider plateau in the longitudinal profile for energy densities [illustrated in Fig. 1(a)]. Without this local rapidity shift, the parameters in Table I will overestimate mid-rapidity charged particle yields in peripheral Au + Au collisions.

At four additional collision energies in the RHIC BES program, measurements of particle rapidity distributions are still very limited. We present our model predictions for the rapidity distributions of final positively charged pions in Fig. 6. Because we utilize the total collision energy as a constraint in our model, we only need to adjust the plateau widths of the initial energy density profiles to match the measured π^+ yields in $|\Delta y| < 0.1$ [45]. Again, we only use the most central 0–5% data for calibrations. Figure 6 shows that the measured centrality dependence of particle production is well predicted by our model. Our predictions for particle rapidity distributions can be compared with future measurements from the RHIC BES phase II program.

We apply the same framework to simulate Pb + Pb collisions at two SPS collision energies. Rapidity distributions of π^- in five centrality bins are compared with the NA49 measurements [46] in Fig. 7. Once calibrated using measurements at the most central 0–5% centrality, our model provides a reasonable description of the π^- rapidity distributions in the remaining four semi-peripheral centrality bins. The widths in π^-'s rapidity distributions at $\sqrt{s_{\rm NN}} = 17.3$ GeV increase slightly faster in the experimental measurements than those in our model calculations.

Last but not least, we test our model's predictive power by simulating highly asymmetric d + Au collisions at four collision energies. We use the same set of model parameters calibrated by central Au + Au collisions at the same collision energy. Figure 8 shows a comparison with the recent PHENIX measurements [47,48]. Our model qualitatively reproduces the collision energy dependence of charged hadron productions at mid-rapidity in d + Au collisions. However, the pseu-

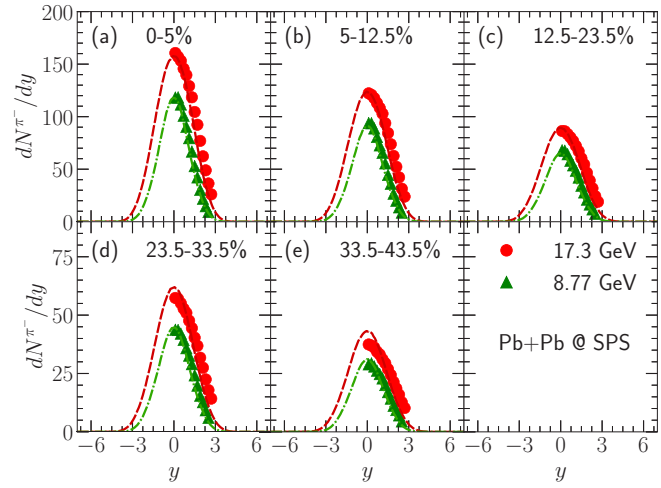

FIG. 7. The rapidity distributions of π^- production compare with the NA49 measurements in Pb + Pb collisions at $\sqrt{s_{\rm NN}} = 17.3$ and 8.77 GeV [46].

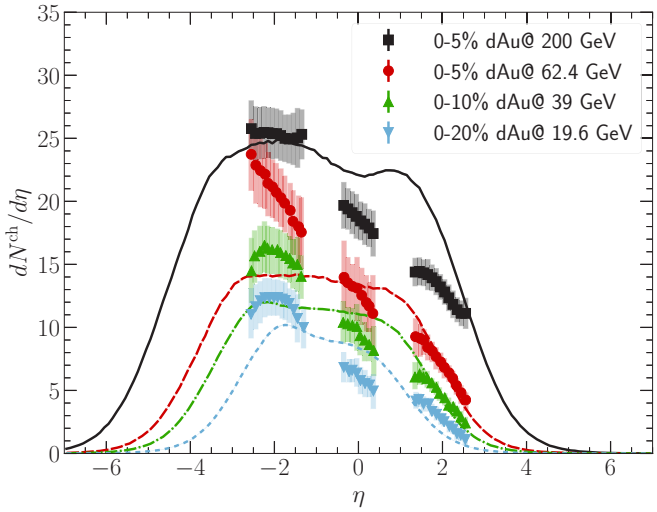

FIG. 8. Model prediction of the charged hadron pseudorapidity distribution in central d + Au collisions. Comparisons are made with the PHENIX measurements for $\sqrt{s} = 19.6$, 39, 62.4, and 200 GeV [47,48].

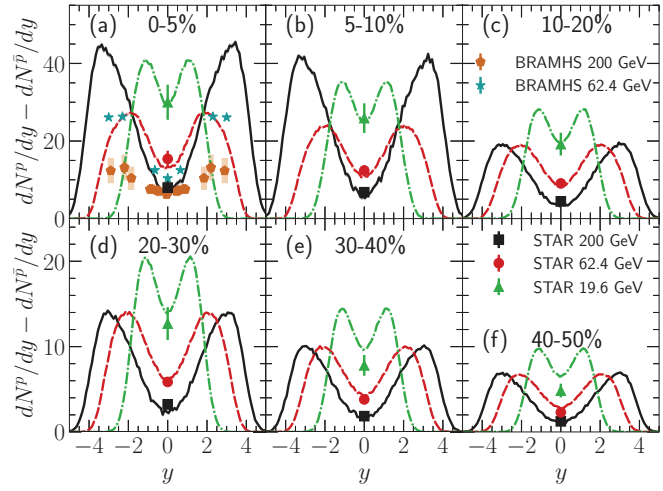

FIG. 9. The net proton rapidity distributions in Au + Au collisions at 19.6, 62.4, and 200 GeV, compared with measurements from the BRAHMS and STAR Collaborations [45,50,51]. Contributions from weak decays are included in the theoretical calculations.

dorapidity distributions are somewhat too flat compared to the PHENIX measurements. These differences could come from the event-by-event fluctuations and/or non-trivial initial longitudinal flow velocity profiles [49], which our current model has ignored.

B. Baryon dynamics and net proton rapidity distributions

Understanding the dynamics of baryon stopping is one of the main topics in the RHIC BES program. In this paper, we parametrize initial baryon distributions with Eqs. (17) and (18). We do not intend to model the detailed baryon stopping mechanism, but rather to provide a parametric fit to all the existing heavy-ion measurements. This calibration makes sure all the collision systems are probing proper regions of the QCD phase diagram. To reduce the number of model parameters, we assume there is no baryon diffusion process during the hydrodynamic phase. The space-time rapidity profile for the initial baryon density is parametrized as the sum of two asymmetric Gaussian profiles for baryon charges carried by the projectile and target nucleus. We calibrated the parameters in Eqs. (17) and (18) with the available net proton measurements in heavy-ion collisions.

Figure 9 show net proton rapidity distributions in Au + Au collisions from 0–5% to 40–50% centrality bin at three collision energies. To compare with the RHIC measurements, we include feed-down contributions from weak decays from heavy resonance states to protons and anti-protons. Net proton distributions were measured by the BRAHMS Collaboration in the most central 0–5% centrality in Au + Au collisions at 200 and 62.4 GeV [50]. The mid-rapidity measurements by the STAR Collaboration [51] are consistent with the BRAHMS results. By adjusting the model parameters in Table I, we can reasonably match the BRAHMS measurements near mid-rapidity. For 19.6 GeV, our model parameters are only guided by the STAR data at $y = 0$. Nevertheless, our model predictions in Figs. 9(b)–9(f) give good descriptions of the STAR measurements in semi-peripheral Au + Au collisions.

At four additional collision energies in the RHIC BES program, rapidity distributions of net proton distributions have not been measured yet. We adjust our model parameters to match the measured net proton yields at mid-rapidity in the central 0–5% Au + Au collisions shown in Fig. 10. Our results in the remaining five centrality bins can be considered as model predictions. We slightly overestimated the mid-rapidity net proton yield in the 40–50% centrality bin, which hints at a weaker baryon stopping in peripheral collisions than central ones.

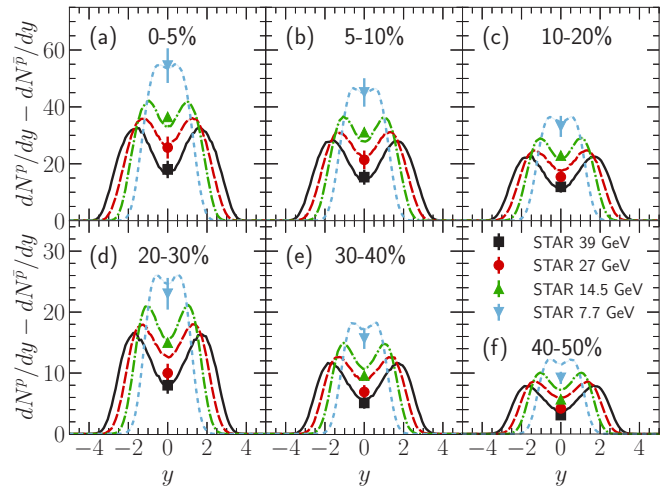

FIG. 10. The net proton rapidity distributions in Au + Au collisions at 7.7, 14.5, 27, and 39 GeV, compared with measurements from the STAR Collaboration at mid-rapidity [45]. Contributions from weak decays are included in the theoretical calculations.

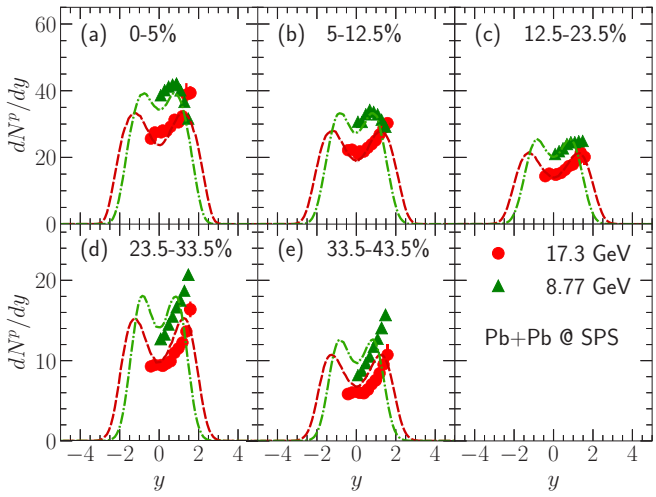

FIG. 11. The proton rapidity distributions in Pb + Pb collisions at $\sqrt{s_{\rm NN}} = 17.3$ and 8.77 GeV, compared with measurements from the NA49 Collaboration [52].

Finally, we study proton rapidity distributions in Pb + Pb collisions at CERN SPS collision energies in Fig. 11. The NA49 Collaboration measured proton rapidity distributions at center-of-mass energies $\sqrt{s_{\rm NN}} = 17.3$ and 8.77 GeV for five centrality bins [52]. Our calculations give an overall good description to the NA49 measurements. Figures 11(d) and 11(e) show that the proton yields keep increasing in forward rapidity regions in semi-peripheral collisions, which is not seen in our calculations. This qualitative difference may suggest that the experimental data have a contamination of protons from the spectators at forward rapidity regions. Our model parameters used to calibrate Pb + Pb collisions at SPS collision energies are consistent with those used in Au + Au collisions at similar RHIC BES energies.

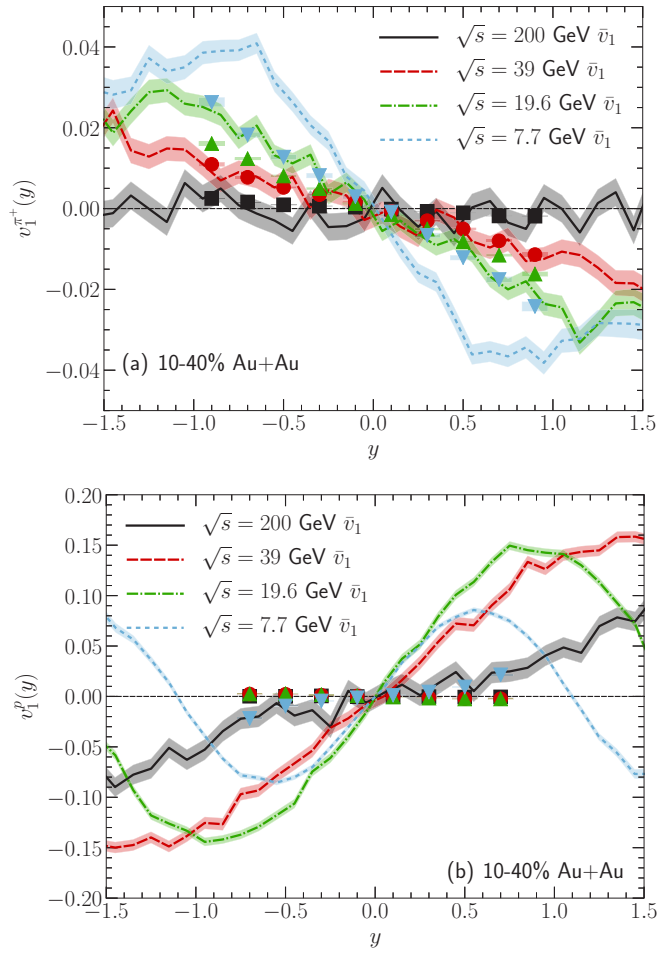

FIG. 12. Identified particle directed flow coefficients for (a) π^+ and (b) protons as functions of rapidity in 10–40% Au + Au collisions at $\sqrt{s_{\rm NN}} = 200$, 39, 19.6, and 7.7 GeV. Comparisons are made with the STAR measurements [53].

C. Rapidity-dependent anisotropic flow

The rapidity distributions of anisotropic flow observables can elucidate the coupling between transverse and longitudinal dynamics in heavy-ion collisions. In this section, we benchmark our results with event-averaged initial conditions, which contain high degrees of symmetry. These flow results can be viewed as a baseline for future comparisons with those from more realistic event-by-event simulations.

Figure 12 shows the rapidity-dependent identified particle directed flow coefficients at four collision energies. The slope of π^+'s directed flow $dv_1^{\pi^+}/dy|_{y=0}$ is negative at mid-rapidity, and its magnitude is larger at lower collision energy. Our simulation shows that the $v_1(y)$ of π^+ follows the dipole deformation of the initial energy density profile in Fig. 2(a). This correlation reflects that the directed flow of π^+ is mainly driven by local pressure gradients, similar to the dynamics of elliptic flow. In the meantime, the proton $v_1(y)$ has an opposite sign compared to that of π^+ at all collision energies. This is because the proton $v_1(y)$ receives additional contributions from initial decelerated baryons other than thermal emissions from fluid cells. These decelerated baryons carry a directed flow pointing to the spectators' direction in the transverse plane.

Our π^+'s directed flow agrees reasonably with the STAR measurements for $\sqrt{s} \geqslant 39$ GeV [53]. They start to overestimate the experimental data at lower collision energies. Our model overestimated the proton's directed flow by more than an order of magnitude. The slopes of proton v_1 are all positive for all collision energies. This failure suggests that our ansatz for initial baryon distributions in Eqs. (17) and (18) is too simple. More realistic modeling of the initial baryon stopping mechanism is needed to understand the RHIC measurements.

Figure 13 further shows pseudorapidity distributions of charged hadron elliptic flow at 14.5 GeV. Our full hybrid simulations with event-averaged initial conditions (the solid black line) give a flatter distribution of $v_2(\eta)$ near mid-rapidity compared to the STAR measurements [54]. Our $v_2(\eta)$ distribution is a result of the cancellation between large effective shear viscosity in large-μ_B regions and large initial eccentricity ε_2 in the forward and backward rapidity regions [see Fig. 2(b)]. Simulations with constant or only temperature-dependent specific shear viscosity give larger charged hadron v_2 at $\eta \approx 2$

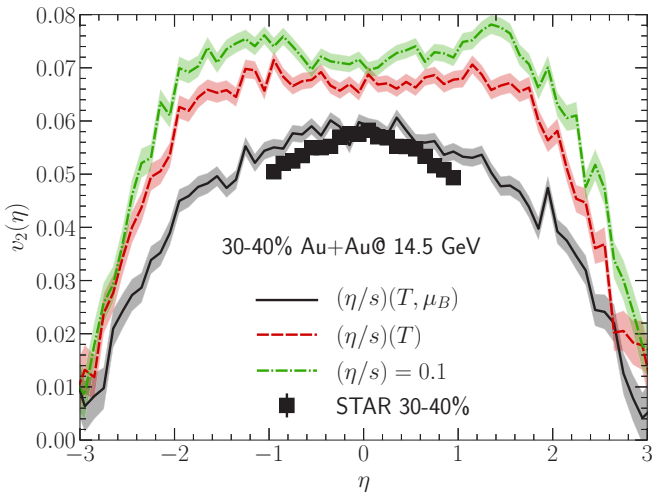

FIG. 13. Pseudorapidity distributions of charged hadron elliptic flow coefficients in 30–40% Au + Au collisions at $\sqrt{s_{\rm NN}} = 14.5$ GeV with different $(\eta/s)(T, \mu_B)$. The charged hadron $v_2(\eta)$ coefficients are integrated from $p_T = 0.2$ to 3 GeV and compared with the STAR measurements [54].

compared to its value at mid-rapidity in Fig. 13. This discrepancy between our full results and the STAR measurements suggests that flow longitudinal decorrelations rooted from event-by-event fluctuations are essential to understand this observable [55]. We devote the extension to event-by-event simulations and studying longitudinal flow fluctuations to a future work.

D. Study QGP transport properties with the $\sqrt{s}$-dependent transverse dynamics

Hydrodynamic flow boosts the thermally emitted hadrons, which results in increasing their mean transverse momenta. In this work, we neglect bulk viscous effects in the QGP evolution and adjust the starting time of hydrodynamics at every collision energy so that identified particles' $\langle p_T \rangle$ match the STAR measurements in 0–5% Au + Au collisions [51,54,56].

Figure 14 shows the identified particle mean p_T as a function of collision energy for 0–5% and 30–40% centrality bins. Our theoretical calculations can quantitatively reproduce the STAR measurements and capture the collision energy dependence of $\langle p_T \rangle$. It is clear from the proton's mean p_T that systems at higher collision energy develop stronger radial flow because their hydrodynamic phases are longer. Our calculation suggests that the mean p_T of anti-protons is larger than that of protons in all collision energies. This difference increases with the net baryon chemical potential at low collision energies. The systematic uncertainties in the current proton and anti-proton measurements are still too large to distinguish them from each other.

Please note that our results ignore any pre-equilibrium dynamics before the hydrodynamic starting time τ_0 listed in Table I. Any pre-hydrodynamic evolution [57–60] will generate transverse flow during $\tau = 0^+ - \tau_0$, which will result in stronger transverse flow at the freeze-out and larger particle mean p_T. This strong radial flow needs to be tamed by

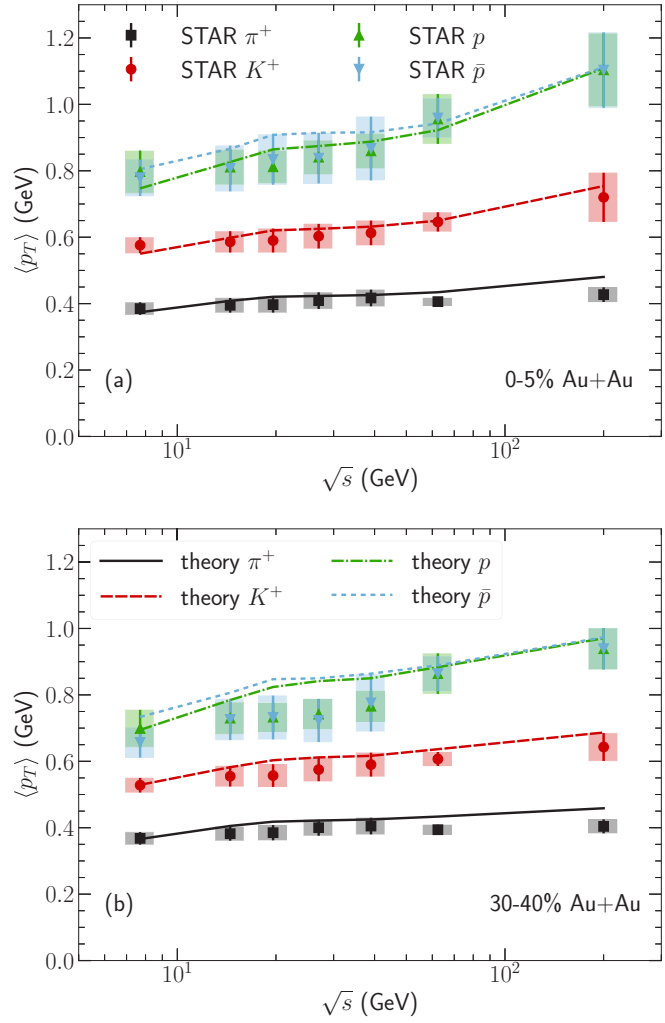

FIG. 14. Collision energy dependence of the identified particle averaged transverse momentum $\langle p_T \rangle$ in Au + Au collisions at (a) 0–5% and (b) 30–40% centrality bins. Theoretical results are compared with the STAR measurements in Refs. [51,54,56].

bulk viscous effects during hydrodynamic evolution [61,62]. Therefore, the fact that our current results can reproduce the STAR mean p_T measurements suggest a non-zero QGP bulk viscosity at finite densities.

In high-energy collisions, the mid-rapidity elliptic flow coefficient of charged hadrons is driven by the fireball's elliptic deformation $\varepsilon_2(\eta_s)$ [63,64]. Although the mid-rapidity $\varepsilon_2^{\rm 3D}(\eta_s = 0)$ for a given centrality class of Au + Au collisions only varies by few percent from 200 to 7.7 GeV, the plateau of $\varepsilon_2(\eta_s)$ shrinks quickly in space-time rapidity as the collision energy goes down [see Fig. 2(b)]. The averaged shape of the fireball in $|\eta_s| < 1$ is more eccentric at a lower collision energy. This larger averaged initial eccentricity is an effect from the breaking of boost invariance in full 3D simulations. The detailed 3D structure of $\varepsilon_2^{\rm 3D}(\eta_s)$ is important for the elliptic flow development during hydrodynamic simulations.

Figure 15(a) shows our model calibration on the STAR elliptic flow measurements with the specific shear viscosity $(\eta/s)(T, \mu_B)$ shown in Fig. 4. Please note that our simulations

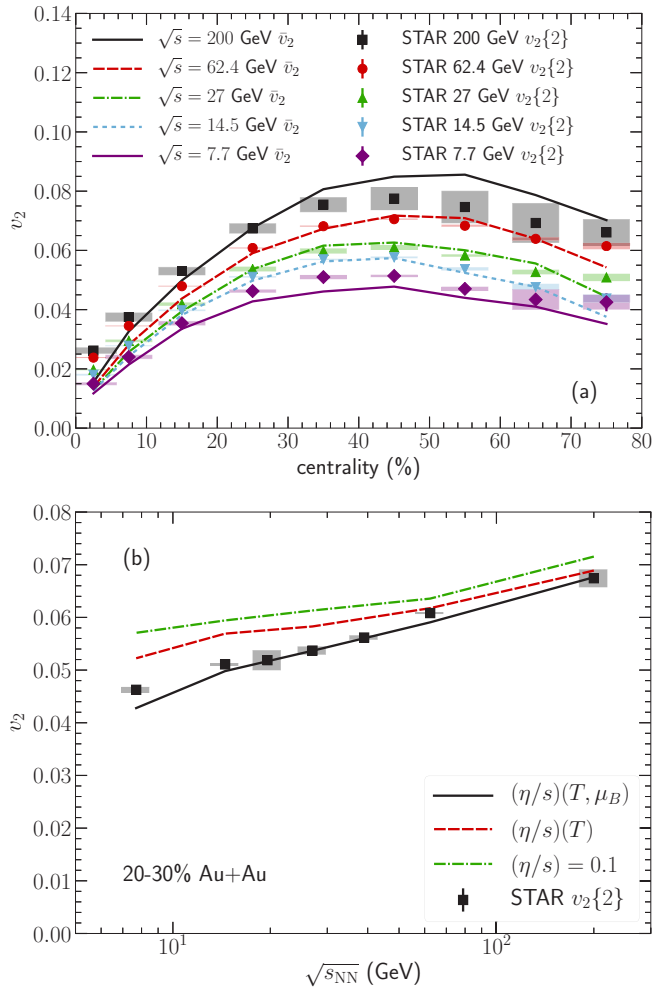

FIG. 15. The dependence of elliptic flow coefficients on (a) collision centrality and (b) collision energy in Au + Au collisions from 7.7 to 200 GeV. Theoretical results are compared with STAR measurements using the two-particle cumulant method [56].

neglect event-by-event fluctuations and bulk viscous effects. Although these two factors give opposite contribution to the elliptic flow coefficient, we expect $\mathcal{O}(20\%)$ theoretical uncertainty in our calculations. Therefore, our following discussion focuses on qualitative features in the model-to-data comparisons. In order to reproduce the collision energy dependence of the STAR elliptic flow measurements, we require a larger QGP specific shear viscosity in the low-T and large-μ_B regions. Our conclusion is in line with the finding in Ref. [19], in which the effective $\eta/s(\sqrt{s})$ is larger at a lower collision energy. We further study individual effects from T and μ_B dependence in η/s on the collision-energy-dependent elliptic flow coefficients in Fig. 15(b). The μ_B dependence in η/s gives a large contribution to the suppression of charged hadron $v_2(\sqrt{s})$ at low collision energies, at which more baryons are stopped at mid-rapidity. Full 3D simulations are essential to extract the T- and μ_B-dependent $\eta/s(T, \mu_B)$. If one assumes systems are boost invariant at all these collision energies, one would need a roughly constant η/s to reproduce the collision energy dependence of charged hadron v_2 [65].

Our results in Figs. 13 and 15 have demonstrated that full 3D dynamics of heavy-ion collisions can set strong constraints on the temperature- and chemical-potential-dependent QGP specific shear viscosity $(\eta/s)(T, \mu_B)$ by using the elliptic flow measurements as functions of particle rapidity and collision energy in the RHIC BES program.

IV. CONCLUSIONS

In this work, we present a simple way to construct 3D initial conditions for relativistic heavy-ion collisions at any energy. The key ingredient is that our formulation ensures local energy and momentum conservation at all transverse positions (x, y) of the system. The conservation laws, together with our choice of the longitudinal energy density profile in Eq. (14), result in a non-trivial $\sqrt{T_A T_B}$ scaling for the local energy density $e(x, y)$ at high energies. This scaling qualitatively agrees with the phenomenological constrained results from state-of-the-art Bayesian statistical analyses [29,30]. Therefore, our work provides an alternative physical interpretation for this type of scaling, in addition to saturation physics [66]. From our model's point of view, the fact that $e \propto \sqrt{T_A T_B}$ is a consequence of longitudinal momentum conservation and the assumption of a flux-tube-like longitudinal profile for the local energy density.

We systematically study these types of 3D initial conditions using a viscous hydrodynamics plus hadronic transport hybrid framework. We calibrate this framework with charged hadron and proton rapidity distributions in most central heavy-ion collisions in the RHIC BES program and at CERN SPS energies. By fixing all the parameters, we test model predictions in semi-peripheral Au + Au and Pb + Pb collisions as well as in asymmetric d + Au collisions. The proposed 3D initial conditions can quantitatively reproduce particle rapidity distributions measured in different centrality bins and in d + Au collisions. These successful predictions support that imposing local energy-momentum conservation plays a critical role in understanding the evolution of charged hadron pseudorapidity distributions as a function of collision geometry in heavy-ion collisions. In the meantime, our model with event-averaged initial conditions failed to describe the rapidity-dependent $v_1(y)$ of pions and protons. These discrepancies indicate that a realistic baryon stopping mechanism and event-by-event fluctuations play critical roles in understanding the directed flow observables.

We further study the collision energy dependence of flow observables at mid-rapidity. Our model without any pre-equilibrium dynamics before $\tau = \tau_0$ can reproduce the measured mean p_T of identified particles. This comparison hints that a non-zero QGP bulk viscosity is essential in the more realistic heavy-ion simulations at finite densities. We demonstrate that the charged hadrons $v_2(\sqrt{s})$ in the RHIC BES program have strong constraining power on the temperature and μ_B dependence of the QGP specific shear viscosity.

The calibrated simulations presented here serve as a baseline result for the bulk dynamics in the RHIC BES program. Future comparisons with more realistic simulations will quantitatively address the importance of event-by-event fluctuations and pre-equilibrium evolution on flow observ-

ables at different collision energies. Last but not least, our calibrated medium evolution in this work can be directly used to study the evolution of critical fluctuations [67–69], the effect of strong electric magnetic fields [70,71], and the QGP electromagnetic radiation in a baryon-rich environment [72,73].

All software used in this work are open source:

(a) IEBE-MUSIC [74] is a fully integrated numerical framework to automate hybrid simulations for relativistic heavy-ion collisions.
(b) SUPERMC [31,32] is an initial condition generator based on the Monte Carlo Glauber model.
(c) MUSIC [35–39] is a (3 + 1)D relativistic viscous hydrodynamics model.
(d) ISS [31,75] is a Monte Carlo particlization module based on the Cooper-Frye freeze-out procedure.
(e) URQMD [42,43,76] is a standard hadronic transport model.
(f) HADRONIC_AFTERBURNER_TOOLKIT [77] is a particle spectra and flow analysis code package.

The event-averaged initial conditions, hydrodynamic hypersurfaces, and final experimental observables can be downloaded from Ref. [78].

ACKNOWLEDGMENTS

The authors thank A. Monnai for giving support on the equation of state and D. Oliinychenko for fruitful discussions. This work is supported under DOE Contract No. DE-SC0013460 and in part by the U.S. Department of Energy, Office of Science, Office of Nuclear Physics, within the framework of the Beam Energy Scan Theory (BEST) Topical Collaboration. S.A. acknowledges scholarship supports from the Department of Physics, Jazan Univeristy, Jazan, Kingdom of Saudi Arabia. This research used resources of the National Energy Research Scientific Computing Center, which is supported by the Office of Science of the U.S. Department of Energy under Contract No. DE-AC02-05CH11231 and resources of the high performance computing services at Wayne State University.

[1] Y. Aoki, G. Endrodi, Z. Fodor, S. D. Katz, and K. K. Szabo, The order of the quantum chromodynamics transition predicted by the standard model of particle physics, Nature (London) **443**, 675 (2006).
[2] M. A. Stephanov, QCD phase diagram and the critical point, Prog. Theor. Phys. Suppl. **153**, 139 (2004).
[3] A. Bzdak, S. Esumi, V. Koch, J. Liao, M. Stephanov, and N. Xu, Mapping the phases of quantum chromodynamics with beam energy scan, Phys. Rep. **853**, 1 (2020).
[4] L. Adamczyk *et al.* (STAR Collaboration), Global Λ hyperon polarization in nuclear collisions: Evidence for the most vortical fluid, Nature (London) **548**, 62 (2017).
[5] C. Shen, Studying QGP with flow: A theory overview, in *Proceedings of the 28th International Conference on Ultra-relativistic Nucleus-Nucleus Collisions* (Quark Matter 2019), Wuhan, China (unpublished), arXiv:2001.11858.
[6] C. Shen and B. Schenke, Dynamical initial state model for relativistic heavy-ion collisions, Phys. Rev. C **97**, 024907 (2018).
[7] B. Alver, M. Baker, C. Loizides, and P. Steinberg, The PHOBOS Glauber Monte Carlo, arXiv:0805.4411.
[8] B. Schenke, P. Tribedy, and R. Venugopalan, Event-by-event gluon multiplicity, energy density, and eccentricities in ultrarelativistic heavy-ion collisions, Phys. Rev. C **86**, 034908 (2012).
[9] H. Mäntysaari and B. Schenke, Evidence of Strong Proton Shape Fluctuations from Incoherent Diffraction, Phys. Rev. Lett. **117**, 052301 (2016).
[10] H. Mäntysaari, B. Schenke, C. Shen, and P. Tribedy, Imprints of fluctuating proton shapes on flow in proton-lead collisions at the LHC, Phys. Lett. B **772**, 681 (2017).
[11] T. Hirano, U. W. Heinz, D. Kharzeev, R. Lacey, and Y. Nara, Hadronic dissipative effects on elliptic flow in ultrarelativistic heavy-ion collisions, Phys. Lett. B **636**, 299 (2006).
[12] P. Bozek, W. Broniowski, and J. Moreira, Torqued fireballs in relativistic heavy-ion collisions, Phys. Rev. C **83**, 034911 (2011).
[13] P. Bozek and W. Broniowski, The torque effect and fluctuations of entropy deposition in rapidity in ultra-relativistic nuclear collisions, Phys. Lett. B **752**, 206 (2016).
[14] W. Broniowski and P. Bożek, Simple model for rapidity fluctuations in the initial state of ultrarelativistic heavy-ion collisions, Phys. Rev. C **93**, 064910 (2016).
[15] P. Bożek, Angle and magnitude decorrelation in the factorization breaking of collective flow, Phys. Rev. C **98**, 064906 (2018).
[16] M. Barej, A. Bzdak, and P. Gutowski, Wounded nucleon, quark and quark-diquark emission functions versus experimental results from RHIC, Phys. Rev. C **100**, 064902 (2019).
[17] G. Denicol, A. Monnai, and B. Schenke, Moving Forward to Constrain the Shear Viscosity of QCD Matter, Phys. Rev. Lett. **116**, 212301 (2016).
[18] L.-G. Pang, G.-Y. Qin, V. Roy, X.-N. Wang, and G.-L. Ma, Longitudinal decorrelation of anisotropic flows in heavy-ion collisions at the CERN Large Hadron Collider, Phys. Rev. C **91**, 044904 (2015).
[19] I. A. Karpenko, P. Huovinen, H. Petersen, and M. Bleicher, Estimation of the shear viscosity at finite net-baryon density from $A + A$ collision data at $\sqrt{s_{\rm NN}} = 7.7$–200 GeV, Phys. Rev. C **91**, 064901 (2015).
[20] L. Du, U. Heinz, and G. Vujanovic, Hybrid model with dynamical sources for heavy-ion collisions at BES energies, Nucl. Phys. A **982**, 407 (2019).
[21] Y. Akamatsu, M. Asakawa, T. Hirano, M. Kitazawa, K. Morita, K. Murase, Y. Nara, C. Nonaka, and A. Ohnishi, Dynamically integrated transport approach for heavy-ion collisions at high baryon density, Phys. Rev. C **98**, 024909 (2018).
[22] C. Shen and B. Schenke, Initial state and hydrodynamic modeling of heavy-ion collisions at RHIC BES energies, Proceedings of the 11th International Workshop on Critical Point and Onset of Deconfinement (CPOD2017), Stony Brook, New York, USA (unpublished), https://doi.org/10.22323/1.311.0006, arXiv:1711.10544.

[23] B. Schenke and S. Schlichting, 3D glasma initial state for relativistic heavy ion collisions, Phys. Rev. C **94**, 044907 (2016).

[24] S. McDonald, S. Jeon, and C. Gale, Exploring longitudinal observables with 3+1D IP-Glasma, arXiv:2001.08636.

[25] M. Li and J. I. Kapusta, Large baryon densities achievable in high energy heavy ion collisions outside the central rapidity region, Phys. Rev. C **99**, 014906 (2019).

[26] L. D. McLerran, S. Schlichting, and S. Sen, Spacetime picture of baryon stopping in the color-glass condensate, Phys. Rev. D **99**, 074009 (2019).

[27] M. Attems, Y. Bea, J. Casalderrey-Solana, D. Mateos, M. Triana, and M. Zilhão, Holographic Collisions Across a Phase Transition, Phys. Rev. Lett. **121**, 261601 (2018).

[28] A. Szczurek, M. Kiełbowicz, and A. Rybicki, Implications of energy and momentum conservation for particle emission in $A + A$ collisions at energies available at the CERN Super Proton Synchrotron, Phys. Rev. C **95**, 024908 (2017).

[29] J. E. Bernhard, J. S. Moreland, S. A. Bass, J. Liu, and U. Heinz, Applying Bayesian parameter estimation to relativistic heavy-ion collisions: Simultaneous characterization of the initial state and quark-gluon plasma medium, Phys. Rev. C **94**, 024907 (2016).

[30] J. E. Bernhard, J. S. Moreland, and S. A. Bass, Bayesian estimation of the specific shear and bulk viscosity of quark-gluon plasma, Nat. Phys. **15**, 1113 (2019).

[31] C. Shen, Z. Qiu, H. Song, J. Bernhard, S. Bass, and U. Heinz, The iEBE-VISHNU code package for relativistic heavy-ion collisions, Comput. Phys. Commun. **199**, 61 (2016).

[32] The SUPERMC code package generates event-by-event and event-averaged initial conditions based on the MC Glauber and the MCKLN models. It can be downloaded from https://github.com/chunshen1987/superMC.

[33] T. Hirano and Y. Nara, Eccentricity fluctuation effects on elliptic flow in relativistic heavy ion collisions, Phys. Rev. C **79**, 064904 (2009).

[34] Z. Qiu and U. W. Heinz, Event-by-event shape and flow fluctuations of relativistic heavy-ion collision fireballs, Phys. Rev. C **84**, 024911 (2011).

[35] G. S. Denicol, C. Gale, S. Jeon, A. Monnai, B. Schenke, and C. Shen, Net baryon diffusion in fluid dynamic simulations of relativistic heavy-ion collisions, Phys. Rev. C **98**, 034916 (2018).

[36] B. Schenke, S. Jeon, and C. Gale, (3+1)D hydrodynamic simulation of relativistic heavy-ion collisions, Phys. Rev. C **82**, 014903 (2010).

[37] B. Schenke, S. Jeon, and C. Gale, Higher flow harmonics from (3+1)D event-by-event viscous hydrodynamics, Phys. Rev. C **85**, 024901 (2012).

[38] J.-F. Paquet, C. Shen, G. S. Denicol, M. Luzum, B. Schenke, S. Jeon, and C. Gale, Production of photons in relativistic heavy-ion collisions, Phys. Rev. C **93**, 044906 (2016).

[39] The official website of MUSIC is https://www.physics.mcgill.ca/music. The latest version of the code can be downloaded from https://github.com/MUSIC-fluid/MUSIC.

[40] A. Monnai, B. Schenke, and C. Shen, Equation of state at finite densities for QCD matter in nuclear collisions, Phys. Rev. C **100**, 024907 (2019).

[41] A. Monnai, B. Schenke, and C. Shen, QCD equation of state at finite densities for nuclear collisions, in Proceedings of the 28th International Conference on Ultrarelativistic Nucleus-Nucleus Collisions (Quark Matter 2019), Wuhan, China (unpublished), arXiv:2002.02661.

[42] S. A. Bass *et al.*, Microscopic models for ultrarelativistic heavy ion collisions, Prog. Part. Nucl. Phys. **41**, 255 (1998).

[43] M. Bleicher *et al.*, Relativistic hadron hadron collisions in the ultrarelativistic quantum molecular dynamics model, J. Phys. G **25**, 1859 (1999).

[44] B. B. Back *et al.* (PHOBOS Collaboration), Charged-particle pseudorapidity distributions in Au+Au collisions at $s(NN)^{1/2} =$ 62.4 GeV, Phys. Rev. C **74**, 021901 (2006).

[45] L. Adamczyk *et al.* (STAR Collaboration), Bulk properties of the medium produced in relativistic heavy-ion collisions from the Beam Energy Scan program, Phys. Rev. C **96**, 044904 (2017).

[46] T. Anticic *et al.* (NA49 Collaboration), System-size and centrality dependence of charged kaon and pion production in nucleus-nucleus collisions at 40*A* GeV and 158*A* GeV beam energy, Phys. Rev. C **86**, 054903 (2012).

[47] A. Adare *et al.* (PHENIX Collaboration), Pseudorapidity Dependence of Particle Production and Elliptic Flow in Asymmetric Nuclear Collisions of $p +$ Al, $p +$ Au, $d +$ Au, and ^{3}He + Au at $\sqrt{s_{NN}} = 200$ GeV, Phys. Rev. Lett. **121**, 222301 (2018).

[48] C. Aidala *et al.* (PHENIX Collaboration), Measurements of azimuthal anisotropy and charged-particle multiplicity in $d +$ Au collisions at $\sqrt{s_{NN}} = 200$, 62.4, 39, and 19.6 GeV, Phys. Rev. C **96**, 064905 (2017).

[49] C. Shen and B. Schenke (unpublished).

[50] I. G. Bearden *et al.* (BRAHMS Collaboration), Nuclear Stopping in Au + Au Collisions at $\sqrt{s_{NN}} = 200$ GeV, Phys. Rev. Lett. **93**, 102301 (2004).

[51] B. I. Abelev *et al.* (STAR Collaboration), Systematic measurements of identified particle spectra in pp, d^+Au, and Au+Au collisions at the STAR detector, Phys. Rev. C **79**, 034909 (2009).

[52] T. Anticic *et al.* (NA49 Collaboration), Centrality dependence of proton and antiproton spectra in Pb+Pb collisions at 40*A* GeV and 158*A* GeV measured at the CERN SPS, Phys. Rev. C **83**, 014901 (2011).

[53] L. Adamczyk *et al.* (STAR Collaboration), Beam-Energy Dependence of the Directed Flow of Protons, Antiprotons, and Pions in Au+Au Collisions, Phys. Rev. Lett. **112**, 162301 (2014).

[54] J. Adam *et al.* (STAR Collaboration), Bulk properties of the system formed in Au+Au collisions at $\sqrt{s_{\rm NN}} = 14.5$ GeV, Phys. Rev. C **101**, 024905 (2020).

[55] A. Behera, M. Nie, and J. Jia, Longitudinal eccentricity decorrelations in heavy ion collisions, Phys. Rev. Res. **2**, 023362 (2020).

[56] L. Adamczyk *et al.* (STAR Collaboration), Harmonic decomposition of three-particle azimuthal correlations at energies available at the BNL Relativistic Heavy Ion Collider, Phys. Rev. C **98**, 034918 (2018).

[57] J. Liu, C. Shen, and U. Heinz, Pre-equilibrium evolution effects on heavy-ion collision observables, Phys. Rev. C **91**, 064906 (2015); **92**, 049904(E) (2015).

[58] A. Kurkela, A. Mazeliauskas, J.-F. Paquet, S. Schlichting, and D. Teaney, Matching the Nonequilibrium Initial Stage of Heavy Ion Collisions to Hydrodynamics with QCD Kinetic Theory, Phys. Rev. Lett. **122**, 122302 (2019).

[59] A. Kurkela, A. Mazeliauskas, J.-F. Paquet, S. Schlichting, and D. Teaney, Effective kinetic description of event-by-event pre-equilibrium dynamics in high-energy heavy-ion collisions, Phys. Rev. C **99**, 034910 (2019).

[60] C. Gale, J.-F. Paquet, B. Schenke, and C. Shen, Probing early-time dynamics and quark-gluon plasma transport properties with photons and hadrons, in Proceedings of the 28th International Conference on Ultrarelativistic Nucleus-Nucleus Collisions (Quark Matter 2019), Wuhan, China (unpblished), arXiv:2002.05191.

[61] S. Ryu, J. F. Paquet, C. Shen, G. S. Denicol, B. Schenke, S. Jeon, and C. Gale, Importance of the Bulk Viscosity of QCD in Ultrarelativistic Heavy-Ion Collisions, Phys. Rev. Lett. **115**, 132301 (2015).

[62] S. Ryu, J.-F. Paquet, C. Shen, G. Denicol, B. Schenke, S. Jeon, and C. Gale, Effects of bulk viscosity and hadronic rescattering in heavy ion collisions at energies available at the BNL Relativistic Heavy Ion Collider and at the CERN Large Hadron Collider, Phys. Rev. C **97**, 034910 (2018).

[63] H. Li and L. Yan, Pseudorapidity dependent hydrodynamic response in heavy-ion collisions, Phys. Lett. B **802**, 135248 (2020).

[64] R. Franco and M. Luzum, Rapidity-dependent eccentricity scaling in relativistic heavy-ion collisions, Phys. Lett. B **806**, 135518 (2020).

[65] C. Shen and U. Heinz, Collision energy dependence of viscous hydrodynamic flow in relativistic heavy-ion collisions, Phys. Rev. C **85**, 054902 (2012); **86**, 049903(E) (2012).

[66] J. S. Moreland, J. E. Bernhard, and S. A. Bass, Alternative ansatz to wounded nucleon and binary collision scaling in high-energy nuclear collisions, Phys. Rev. C **92**, 011901(R) (2015).

[67] M. Stephanov and Y. Yin, Hydrodynamics with parametric slowing down and fluctuations near the critical point, Phys. Rev. D **98**, 036006 (2018).

[68] K. Rajagopal, G. Ridgway, R. Weller, and Y. Yin, Hydro+ in action: Understanding the out-of-equilibrium dynamics near a critical point in the QCD phase diagram, arXiv:1908.08539.

[69] X. An, G. Başar, M. Stephanov, and H.-U. Yee, Fluctuation dynamics in a relativistic fluid with a critical point, arXiv:1912.13456.

[70] U. Gürsoy, D. Kharzeev, E. Marcus, K. Rajagopal, and C. Shen, Charge-dependent flow nduced by magnetic and electric fields in heavy ion collisions, Phys. Rev. C **98**, 055201 (2018).

[71] U. Gürsoy, D. E. Kharzeev, E. Marcus, K. Rajagopal, and C. Shen, Charge-dependent flow induced by electromagnetic fields in heavy ion collisions, arXiv:2002.12818.

[72] C. Gale, S. Jeon, S. McDonald, J.-F. Paquet, and C. Shen, Photon radiation from heavy-ion collisions in the $\sqrt{s_{NN}} = 19$–200 GeV regime, Nucl. Phys. A **982**, 767 (2019).

[73] G. Vujanovic, J.-F. Paquet, C. Shen, G. S. Denicol, S. Jeon, C. Gale, and U. Heinz, Exploring the influence of bulk viscosity of QCD on dilepton tomography, Phys. Rev. C **101**, 044904 (2020).

[74] The IEBE-MUSIC is a generic framework, which integrates multi-stage dynamics to simulate relativistic heavy-ion collisions. It can be downloaded from https://github.com/chunshen1987/iEBE-MUSIC.

[75] The ISS code package can be downloaded from https://github.com/chunshen1987/iSS.

[76] URQMD collaboration, Ultra-relativistic quantum molecular dynamics, 2015, http://urqmd.org.

[77] The HADRONIC_AFTERBURNER_TOOLKIT code package performs particle spectra and anisotropic flow analysis using outputs from hadronic transport models. It can be downloaded from https://github.com/chunshen1987/hadronic_afterburner_toolkit.

[78] Results presented in this paper can be downloaded from https://drive.google.com/drive/folders/1DMml4IXXcilEZaaTpGF2HM_2ICmeydpz?usp=sharing.